New high-speed centre of mass method incorporating background subtraction for accurate determination of fluorescence lifetime

Poland, Simon P.; Erdogan, Ahmet T.; Krstajić, Nikola; Levitt, James; Devauges, Viviane; Walker, Richard J.

Published in:
Optics Express

DOI:
10.1364/OE.24.006899

Publication date:
2016

Document Version
Publisher's PDF, also known as Version of record

New high-speed centre of mass method incorporating background subtraction for accurate determination of fluorescence lifetime

Simon P. Poland,[1,2,*] Ahmet T. Erdogan,[3] Nikola Krstajić,[3,4] James Levitt,[1,2] Viviane Devauges,[1,2] Richard J. Walker,[3,5] David Day-Uei Li,[6] Simon M. Ameer-Beg[1,2] and Robert K. Henderson[3]

[1]*Division of Cancer Studies, Guy's Campus, Kings College, London, UK*
[2]*Randall Division of Cell and Molecular Biophysics, Guy's Campus, Kings College, London, UK*
[3]*Institute for Integrated Micro and Nano Systems, School of Engineering, University of Edinburgh, Edinburgh, UK*
[4]*EPSRC IRC "Hub" in Optical Molecular Sensing & Imaging, MRC Centre for Inflammation Research, Queen's Medical Research Institute, 47 Little France Crescent, University of Edinburgh, Edinburgh EH16 4TJ, UK*
[5]*Photon-Force Ltd., Edinburgh, UK*
[6]*Strathclyde Institute of Pharmacy and Biomedical Sciences, 161 Cathedral Street, Glasgow, G4 0RE, UK*
[*]*simon.poland@gmail.com*

Abstract: We demonstrate an implementation of a centre-of-mass method (CMM) incorporating background subtraction for use in multifocal fluorescence lifetime imaging microscopy to accurately determine fluorescence lifetime in live cell imaging using the Megaframe camera. The inclusion of background subtraction solves one of the major issues associated with centre-of-mass approaches, namely the sensitivity of the algorithm to background signal. The algorithm, which is predominantly implemented in hardware, provides real-time lifetime output and allows the user to effectively condense large amounts of photon data. Instead of requiring the transfer of thousands of photon arrival times, the lifetime is simply represented by one value which allows the system to collect data up to limit of pulse pile-up without any limitations on data transfer rates. In order to evaluate the performance of this new CMM algorithm with existing techniques (i.e. rapid lifetime determination and Levenburg-Marquardt), we imaged live MCF-7 human breast carcinoma cells transiently transfected with FRET standards. We show that, it offers significant advantages in terms of lifetime accuracy and insensitivity to variability in dark count rate (DCR) between Megaframe camera pixels. Unlike other algorithms no prior knowledge of the expected lifetime is required to perform lifetime determination. The ability of this technique to provide real-time lifetime readout makes it extremely useful for a number of applications.

OCIS codes: (180.2520) Fluorescence microscopy; (040.1240) Arrays; (050.1970) Diffractive optics; (180.4315) Nonlinear microscopy.

References and links

1. J. R. Morris, C. Boutell, M. Keppler, R. Densham, D. Weekes, A. Alamshah, L. Butler, Y. Galanty, L. Pangon, T. Kiuchi, T. Ng, and E. Solomon, "The SUMO modification pathway is involved in the BRCA1 response to genotoxic stress," Nature **462**(7275), 886–890 (2009).
2. M. Peter, S. M. Ameer-Beg, M. K. Hughes, M. D. Keppler, S. Prag, M. Marsh, B. Vojnovic, and T. Ng, "Multiphoton-FLIM quantification of the EGFP-mRFP1 FRET pair for localization of membrane receptor-kinase interactions," Biophys. J. **88**(2), 1224–1237 (2005).
3. T. Ng, A. Squire, G. Hansra, F. Bornancin, C. Prevostel, A. Hanby, W. Harris, D. Barnes, S. Schmidt, H. Mellor, P. I. H. Bastiaens, and P. J. Parker, "Imaging protein kinase Calpha activation in cells," Science **283**(5410), 2085–2089 (1999).
4. E. Gratton, S. Breusegem, J. Sutin, Q. Ruan, and N. Barry, "Fluorescence lifetime imaging for the two-photon microscope: time-domain and frequency-domain methods," J. Biomed. Opt. **8**(3), 381–390 (2003).

#256784 Received 5 Jan 2016; revised 15 Feb 2016; accepted 5 Mar 2016; published 21 Mar 2016

5. A. Esposito, H. C. Gerritsen, and F. S. Wouters, "Optimizing frequency-domain fluorescence lifetime sensing for high-throughput applications: photon economy and acquisition speed," J. Opt. Soc. Am. A **24**(10), 3261–3273 (2007).
6. D. M. Grant, J. McGinty, E. J. McGhee, T. D. Bunney, D. M. Owen, C. B. Talbot, W. Zhang, S. Kumar, I. Munro, P. M. P. Lanigan, G. T. Kennedy, C. Dunsby, A. I. Magee, P. Courtney, M. Katan, M. A. A. Neil, and P. M. W. French, "High speed optically sectioned fluorescence lifetime imaging permits study of live cell signaling events," Opt. Express **15**(24), 15656–15673 (2007).
7. T. Omer, L. Zhao, X. Intes, and J. Hahn, "Reduced temporal sampling effect on accuracy of time-domain fluorescence lifetime Förster resonance energy transfer," J. Biomed. Opt. **19**(8), 086023 (2014).
8. A. Leray, S. Padilla-Parra, J. Roul, L. Héliot, and M. Tramier, "Spatio-Temporal Quantification of FRET in living cells by fast time-domain FLIM: a comparative study of non-fitting methods [corrected]," PLoS One **8**(7), e69335 (2013).
9. A. C. Mitchell, J. E. Wall, J. G. Murray, and C. G. Morgan, "Measurement of nanosecond time-resolved fluorescence with a directly gated interline CCD camera," J. Microsc. **206**(3), 233–238 (2002).
10. A. Miyawaki, O. Griesbeck, R. Heim, and R. Y. Tsien, "Dynamic and quantitative Ca2+ measurements using improved cameleons," Proc. Natl. Acad. Sci. U.S.A. **96**(5), 2135–2140 (1999).
11. Q. S. Hanley, V. Subramaniam, D. J. Arndt-Jovin, and T. M. Jovin, "Fluorescence lifetime imaging: multi-point calibration, minimum resolvable differences, and artifact suppression," Cytometry **43**(4), 248–260 (2001).
12. R. A. Colyer, G. Scalia, I. Rech, A. Gulinatti, M. Ghioni, S. Cova, S. Weiss, and X. Michalet, "High-throughput FCS using an LCOS spatial light modulator and an 8 × 1 SPAD array," Biomed. Opt. Express **1**(5), 1408–1431 (2010).
13. X. Michalet, R. A. Colyer, G. Scalia, A. Ingargiola, R. Lin, J. E. Millaud, S. Weiss, O. H. Siegmund, A. S. Tremsin, J. V. Vallerga, A. Cheng, M. Levi, D. Aharoni, K. Arisaka, F. Villa, F. Guerrieri, F. Panzeri, I. Rech, A. Gulinatti, F. Zappa, M. Ghioni, and S. Cova, "Development of new photon-counting detectors for single-molecule fluorescence microscopy," Philos. Trans. R. Soc. Lond. B Biol. Sci. **368**(1611), 20120035 (2012).
14. S. P. Poland, N. Krstajić, S. Coelho, D. Tyndall, R. J. Walker, V. Devauges, P. E. Morton, N. S. Nicholas, J. Richardson, D. D.-U. Li, K. Suhling, C. M. Wells, M. Parsons, R. K. Henderson, and S. M. Ameer-Beg, "Time-resolved multifocal multiphoton microscope for high speed FRET imaging in vivo," Opt. Lett. **39**(20), 6013–6016 (2014).
15. S. P. Poland, N. Krstajić, J. Monypenny, S. Coelho, D. Tyndall, R. J. Walker, V. Devauges, J. Richardson, N. Dutton, P. Barber, D. D. Li, K. Suhling, T. Ng, R. K. Henderson, and S. M. Ameer-Beg, "A high speed multifocal multiphoton fluorescence lifetime imaging microscope for live-cell FRET imaging," Biomed. Opt. Express **6**(2), 277–296 (2015).
16. J. Richardson, R. Walker, L. Grant, D. Stoppa, F. Borghetti, E. Charbon, M. Gersbach, and R. K. Henderson, "A 32x32 50ps Resolution 10 bit Time to Digital Converter Array in 130nm CMOS for Time Correlated Imaging," IEEE Cust. Integr. Cir. **9**, 77–80 (2009).
17. D.-U. Li, B. Rae, R. Andrews, J. Arlt, and R. Henderson, "Hardware implementation algorithm and error analysis of high-speed fluorescence lifetime sensing systems using center-of-mass method," J. Biomed. Opt. **15**, 017006 (2010).
18. L. Marcu, "Fluorescence lifetime techniques in medical applications," Ann. Biomed. Eng. **40**(2), 304–331 (2012).
19. J. Nedbal, V. Visitkul, E. Ortiz-Zapater, G. Weitsman, P. Chana, D. R. Matthews, T. Ng, and S. M. Ameer-Beg, "Time-domain microfluidic fluorescence lifetime flow cytometry for high-throughput Förster resonance energy transfer screening," Cytometry A **87**(2), 104–118 (2015).
20. V. C. Abraham, D. L. Taylor, and J. R. Haskins, "High content screening applied to large-scale cell biology," Trends Biotechnol. **22**(1), 15–22 (2004).
21. D. R. Matthews, G. O. Fruhwirth, G. Weitsman, L. M. Carlin, E. Ofo, M. Keppler, P. R. Barber, I. D. Tullis, B. Vojnovic, T. Ng, and S. M. Ameer-Beg, "A multi-functional imaging approach to high-content protein interaction screening," PLoS One **7**(4), e33231 (2012).
22. R. M. Ballew and J. Demas, "An error analysis of the rapid lifetime determination method for the evaluation of single exponential decays," Anal. Chem. **61**(1), 30–33 (1989).
23. K. K. Sharman, A. Periasamy, H. Ashworth, and J. N. Demas, "Error analysis of the rapid lifetime determination method for double-exponential decays and new windowing schemes," Anal. Chem. **71**(5), 947–952 (1999).
24. S. P. Chan, Z. J. Fuller, J. N. Demas, and B. A. DeGraff, "Optimized gating scheme for rapid lifetime determinations of single-exponential luminescence lifetimes," Anal. Chem. **73**(18), 4486–4490 (2001).
25. C. Moore, S. P. Chan, J. N. Demas, and B. A. DeGraff, "Comparison of methods for rapid evaluation of lifetimes of exponential decays," Appl. Spectrosc. **58**(5), 603–607 (2004).
26. I. Munro, J. McGinty, N. Galletly, J. Requejo-Isidro, P. M. Lanigan, D. S. Elson, C. Dunsby, M. A. Neil, M. J. Lever, and G. W. Stamp, "Toward the clinical application of time-domain fluorescence lifetime imaging," J. Biomed. Opt. **10**, 051403 (2005).
27. A. C. Mitchell, J. E. Wall, J. G. Murray, and C. G. Morgan, "Measurement of nanosecond time-resolved fluorescence with a directly gated interline CCD camera," J. Microsc. **206**(3), 233–238 (2002).
28. R. A. Colyer, O. H. Siegmund, A. S. Tremsin, J. V. Vallerga, S. Weiss, and X. Michalet, "Phasor imaging with a widefield photon-counting detector," J. Biomed. Opt. **17**(1), 016008 (2012).

#256784 Received 5 Jan 2016; revised 15 Feb 2016; accepted 5 Mar 2016; published 21 Mar 2016

29. D. D.-U. Li, J. Arlt, D. Tyndall, R. Walker, J. Richardson, D. Stoppa, E. Charbon, and R. K. Henderson, "Video-rate fluorescence lifetime imaging camera with CMOS single-photon avalanche diode arrays and high-speed imaging algorithm," J. Biomed. Opt. **16**, 096012 (2011).
30. D. D. U. Li, S. Ameer-Beg, J. Arlt, D. Tyndall, R. Walker, D. R. Matthews, V. Visitkul, J. Richardson, and R. K. Henderson, "Time-Domain Fluorescence Lifetime Imaging Techniques Suitable for Solid-State Imaging Sensor Arrays," Sensors (Basel) **12**(5), 5650–5669 (2012).
31. D. D.-U. Li, H. Yu, and Y. Chen, "Fast bi-exponential fluorescence lifetime imaging analysis methods," Opt. Lett. **40**(3), 336–339 (2015).
32. N. Krstajić, J. Levitt, S. Poland, S. Ameer-Beg, and R. Henderson, "256 × 2 SPAD line sensor for time resolved fluorescence spectroscopy," Opt. Express **23**(5), 5653–5669 (2015).
33. S. P. Poland, N. Krstajić, R. D. Knight, R. K. Henderson, and S. M. Ameer-Beg, "Development of a doubly weighted Gerchberg-Saxton algorithm for use in multibeam imaging applications," Opt. Lett. **39**(8), 2431–2434 (2014).
34. G. C. Spalding, J. Courtial, and R. Leonardo, "Structured Light and its Applications," in *Holographic Optical Tweezers* (Academic Press, 2008), pp. 139–168.
35. "Opal Kelly XEM 3050 user manual," (2006), *http://assets00.opalkelly.com/library/XEM3050-UM.pdf*.
36. P. Barber, S. Ameer-Beg, J. Gilbey, L. Carlin, M. Keppler, T. Ng, and B. Vojnovic, "Multiphoton time-domain fluorescence lifetime imaging microscopy: practical application to protein–protein interactions using global analysis," J. R. Soc. Interface **6**(Suppl_1), S93–S105 (2009).
37. D. R. Matthews, G. O. Fruhwirth, G. Weitsman, L. M. Carlin, E. Ofo, M. Keppler, P. R. Barber, I. D. Tullis, B. Vojnovic, T. Ng, and S. M. Ameer-Beg, "A multi-functional imaging approach to high-content protein interaction screening," PLoS One **7**(4), e33231 (2012).
38. H. D. Soule, J. Vazguez, A. Long, S. Albert, and M. Brennan, "A human cell line from a pleural effusion derived from a breast carcinoma," J. Natl. Cancer Inst. **51**(5), 1409–1416 (1973).
39. T. A. Masters, R. J. Marsh, D. A. Armoogum, N. Nicolaou, B. Larijani, and A. J. Bain, "Restricted State Selection in Fluorescent Protein Förster Resonance Energy Transfer," J. Am. Chem. Soc. **135**(21), 7883–7890 (2013).

1. Introduction

The use of fluorescence lifetime imaging microscopy (FLIM) for studying spatio-temporal protein-protein interactions in situ by the detection of FRET between protein-bound fluorophores is well-established [1–3]. For intermolecular FRET, a key advantage of using donor FLIM is that fluorescence lifetime measurements of donor emission are independent of acceptor concentration and is thus suited to studies that explore biological interactions in intact cells and tissues.

For high precision FLIM, time-correlated single photon counting (TCSPC) is unparalleled in its measurement accuracy particularly for multi-exponential decays [4, 5]. Conventional TCSPC is fundamentally limited with respect to photon counting rate in current implementations of laser scanning microscopy, with typical acquisition rates for conventional laser scanning TCSPC FLIM are in the order of minutes [4]. This partly explains why its application is not more widespread in the biomedical community. Until recently high speed FLIM could only be performed using modulated or time-gated image intensifier systems [6–8]. Whilst such systems offer video frame rate acquisitions, they suffer from significant imaging artefacts [9] and excitation photon flux that may be damaging to cells [10–13].

We have recently demonstrated a multifocal fluorescence lifetime imaging microscopy for multiphoton (MM-FLIM) applications [14, 15] which significantly improves the acquisition rate of high resolution fluorescence lifetime imaging by parallelizing excitation and detection. The system consists of a two dimensional array of ultrafast beams (generated using a spatial light modulator) which are then optically conjugated with a Megaframe camera [16] consisting of 32 × 32 individual 10-bit time-to-digital convertor (TDC) array with integrated single-photon avalanche diodes (SPADs), each of which operates in TCSPC mode and provides FLIM capability. Essentially, the microscope system consists of up to 1024 individual multiphoton fluorescence lifetime imaging microscopes working in parallel to enable high data acquisition rates. With this system we have shown the ability to acquire data at sub-second acquisition speeds, imaging both live cell interactions and in vivo [14, 15].

This technique represents a paradigm shift whereby there is no longer a compromise between temporal accuracy, speed and spatial resolution depending on the FLIM system used.

#256784 Received 5 Jan 2016; revised 15 Feb 2016; accepted 5 Mar 2016; published 21 Mar 2016

It demonstrates practical application of fluorescence lifetime imaging for dynamic biological systems on time-scales of relevance to biological processes (sub-seconds) using a technique with sufficient lifetime resolution to resolve minute changes in protein association. Existing frequency domain or time-gating methods simply do not have the quantitative resolution at the speeds required [4].

Two issues presently associated with the MM-FLIM TCSPC approach are (a) limitations in data transfer rates of raw data from the Megaframe camera to the computer and (b) the delay from acquisition of the data set to determination of the associated lifetime values. Although each individual SPAD in the array is capable of measuring a count rate of up to 30MHz, there are limitations to the number of counts which can be transmitted via USB2 (~20MHz count rate assuming each count contains 16-bits of information). If one were to factor in issues such as pulse pile-up (which require photon count rate of the order < 1% of the repetition rate of the laser), one could achieve 0.8MHz/pixel for an 80 MHz laser if transfer rates were not an issue [14]. It is also computationally expensive to sort large data sets into histograms and perform lifetime determination analysis (usually with a non-linear least squares fitting approach i.e. Levenburg-Marquardt). In practice, although data can be acquired quite rapidly with no delay between acquisitions, sorting and analysis is usually performed offline which means that one cannot readily achieve real-time lifetime readouts [17]. Whilst this immediate lifetime analysis is not required in most cases, it could be extremely important in some instances such as medical diagnostics [18], in flow cytometry [19] and high content screening applications [20, 21].

In comparison to iterative fitting approaches, several rapid lifetime determination (RLD) methods [22–26] (i.e time-gating) have been developed to reduce the complexity and thus the time taken to generate a lifetime image. Systems using gating algorithms are widely used due to the ease of implementation with hardware such as time-gated image intensifiers. Whilst useful for providing a preview of the associated lifetime distribution several studies have shown that time gating techniques are somewhat inaccurate due to the introduction of significant image artefacts [27] and sensitivity issues [28].

One non-fitting approach for single exponential decays which has shown a marked improvement over other conventional RLD techniques is the centre-of-mass method (CMM) [29]. This high speed algorithm has previously been implemented on-FPGA with the Megaframe camera for widefield FLIM based applications [30]. A number of variants of this algorithm have since been proposed which provide a more accurate determination for multi-exponential lifetime decays [31].

CMM also allows the user to effectively condense large amounts of photon data. Instead of requiring the transfer of thousands of photon arrival times, the lifetime is simply represented by one value which allows the system to collect data up to limit of pulse pile up without any limitations on data transfer rates.

One problem when using these CMM implementations on the Megaframe camera is the sensitivity of the algorithm to the characteristics of individual detectors. The presence of any background signal biases the centre-of-mass towards the centre of the time-window and thereby skews the determined lifetime value. Whilst recent advances in the SPAD design using the 0.13 μm CMOS fabrication process have led to development of SPAD arrays with predominantly low dark count rates (DCR) [16], when operating the Megaframe camera at 25°C there would still usually be a small number of pixels randomly positioned in the array which have a much higher DCR than the average (see Fig. 1).

#256784 Received 5 Jan 2016; revised 15 Feb 2016; accepted 5 Mar 2016; published 21 Mar 2016

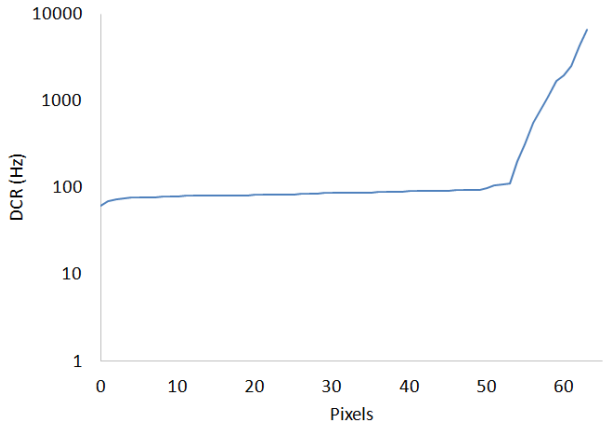

Fig. 1. Dark Count Rate (DCR) of a selected 8x8 detector array on the Megaframe 32x32 pixel camera.

In this paper, we present an implementation of CMM for use in laser scanning microscopy which incorporates background subtraction to compensate for both background signal and variability in sensitivity between individual pixels. Predominantly performed on-FPGA, the algorithm incorporates a second measurement integration window located before the transient to determine the background from the pre-pulse signal. The algorithm also takes into account variability in instrument response functions (IRF) between each pixel utilizing the CMM_{diff} approach to provide a more accurate lifetime determination [32]. This CMM implementation incorporates x-address and y-address signals which are externally triggered to allow synchronization and sorting with the galvanometer scanning. The algorithm, which is predominantly implemented in hardware, provides real-time lifetime output and in terms of data transfer rates is only constrained by the limitations imposed to prevent pulse pile up. Whilst not the most accurate method for determining lifetime it is suitable for certain instances where a fast preview of the lifetime is required.

2. Theory of centre of mass method (CMM)

As shown previously [29] the lifetime τ_{CMM} for a single exponential decay $f(t) = Aexp(-t/\tau)$ for measurement window $0 \le t \le T$ is determined from the equation:

$$\tau = \Omega\left[\frac{1}{M}\left(\frac{\sum_{i=1}^{N_c}\overline{D_i}}{N_c}+\frac{1}{2}\right)\right].Mh \qquad (1)$$

where M represents the number of time bins in the measurement window, D_i is the 10-bit TDC output of the *i*th captured photon, N_c is the total number of photons, h is the time interval size and Ω is the look-up table (LUT) that maps normalised τ_{CMM} to τ. In this previous iteration of the CMM (known as $CMM_{original}$), the time window size M is determined by the FIRST and LAST bin position settings. With the values for M and h known, the on-chip element of the algorithm determines the sum of D_i values, and the total number of photons N_c for each pixel and the τ_{CMM} can be easily calculated.

For the background subtracted CMM algorithm proposed in this paper $CMM_{diffsub}$, a second measurement window placed within the pre-pulse zone is used to sample the background signal level. Whilst the size of this window is relatively small in comparison to the number of bins used to calculate the CMM, since we are only collecting pre-pulse data, the whole scanned data set associated with each individual SPAD detector can be used to

#256784 Received 5 Jan 2016; revised 15 Feb 2016; accepted 5 Mar 2016; published 21 Mar 2016

determine the average background value. For an image of size 256x256 with 8x8 detectors, this equates to the average of 1024 time windows, which gives a much more accurate determination of the background. Once the average background level has been calculated its contribution to the CMM can be subtracted using the equation:

$$\tau = \Omega\left[\frac{1}{M}\left(\frac{\sum_{i=1}^{N_c}\overline{D_i} - \sum^{N_c}\left(\frac{N_b}{S}\right)}{N_c - \left(\frac{N_b}{S}\right)} + \frac{1}{2}\right)\right].Mh \tag{2}$$

where N_b and S represent the total number of photons and the number of bins respectively in the background sampling measurement window. With the values for M, h and S preset by the user, the on-chip element of the algorithm determines the sum of Di values, Nc and Nb for each pixel and the τ_{CMM} can be easily calculated.

2.1 Differential centre-of-mass method (CMM_{diff})

In previous iterations of the CMM for lifetime determination, the lifetime was calculated from a user-defined pre-selected histogram measurement window [29]. The start and end of this measurement window were set to provide best photon efficiency. Precise positioning of the start point was made according to the peak of the average Instrument Response Function (IRF) across all of the detectors. Whilst this allows a lifetime to be determined with little information required, it does not take into account the variability in IRFs between individual pixels. As each pixel on the Megaframe camera has its own SPAD and TDC, they are physically distinct which gives rise to different characteristics. In order to calculate the CMM_{diff} one uses the full measurement window and the τ_{IRF} associated with each individual pixel is simply subtracted from the sample lifetime τ_s as shown in the equation below:

$$\tau_{diff} = \tau_s - \tau_{IRF} \tag{3}$$

This provides a much more accurate determination of the lifetime.

3. Methods

3.1 Optical setup

A schematic of the optical system can be found in Fig. 2. Light from the Ti:Sapphire femtosecond pulsed laser source (Chameleon Ultra II [Coherent Inc.]) is projected onto a Spatial Light Modulator (SLM) [MeadowLark Inc.] which generates a uniform beamlet array in the focal plane using a Doubly Weighted Gerchberg-Saxton algorithm (DWGS) [33].

The 8 × 8 beamlet array is then relayed through a pair of galvanometer scanners (to provide x- and y- scanning) and transmitted through a long-pass dichroic filter onto the back aperture of a x40 1.3 N.A. Plan Fluor oil immersion microscope objective [Nikon Instruments Ltd] where it is then projected onto the sample. Two photon excited fluorescence was then collected from the focal plane by the objective, de-scanned by the galvanometer scanners and re-imaged via a dichroic mirror onto the back aperture of a x10 0.3 N.A. Plan Fluor objective [Nikon] and focused onto the Megaframe SPAD array.

#256784 Received 5 Jan 2016; revised 15 Feb 2016; accepted 5 Mar 2016; published 21 Mar 2016

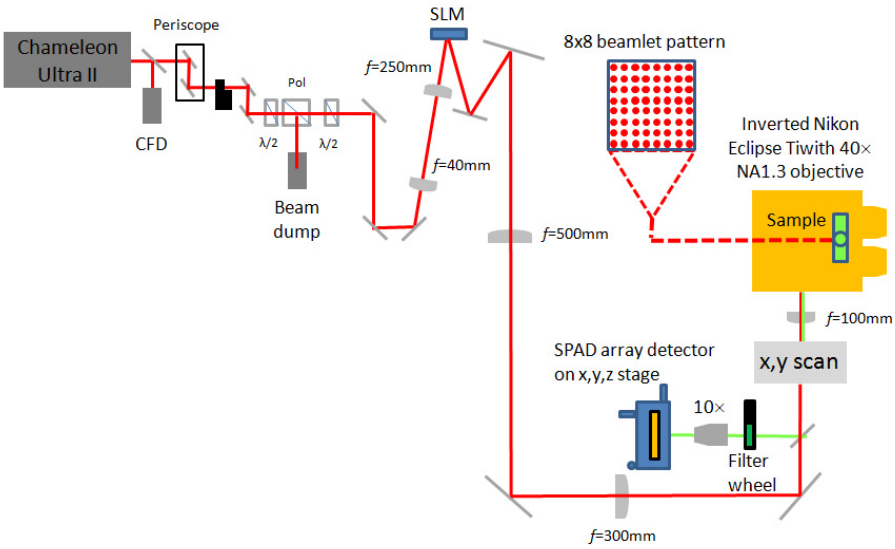

Fig. 2. Operational schematic of the multifocal multiphoton system, whereby light from the Chameleon Ultra II Ti:Sapphire laser system is projected onto the Spatial Light Modulator (SLM) that generates the appropriate beamlet array pattern, which is then re-imaged and scanned across sample and using a set of galvanometers. The two photon generated fluorescence collected by the objective lens is then de-scanned and projected onto the Megaframe SPAD array for detection.

3.2 Calibration and optimization of the MM-FLIM system

Illumination, sample and detection planes were all critically aligned conjugate such that magnification between planes was optimal for both imaging resolution and detection efficiency. Precise alignment and matching of the beamlet spacing and angular orientation onto the detector array was performed to ensure an effective fill factor of 100%. In order to compensate for poor intensity fidelity between beamlets [34], the DWGS algorithm [33] was implemented (incorporating direct feedback from the detector array), leading to significant improvement in uniformity of the beamlet intensity variation.

3.3 TCSPC system architecture

A typical Megaframe camera (MF32) based Time Correlated Single Photon Counting (TCSPC) system block diagram is shown in Fig. 3. The key parts of this system are an application board, a computer, a laser source and a laser scanner. The application board hosts the Megaframe camera and the Opal Kelly FPGA board (XEM3050) which contains the Spartan 3 FPGA from Xilinx and provides a USB2 interface to the computer. The application board also provides interface to a laser source and a laser scanner.

#256784 Received 5 Jan 2016; revised 15 Feb 2016; accepted 5 Mar 2016; published 21 Mar 2016

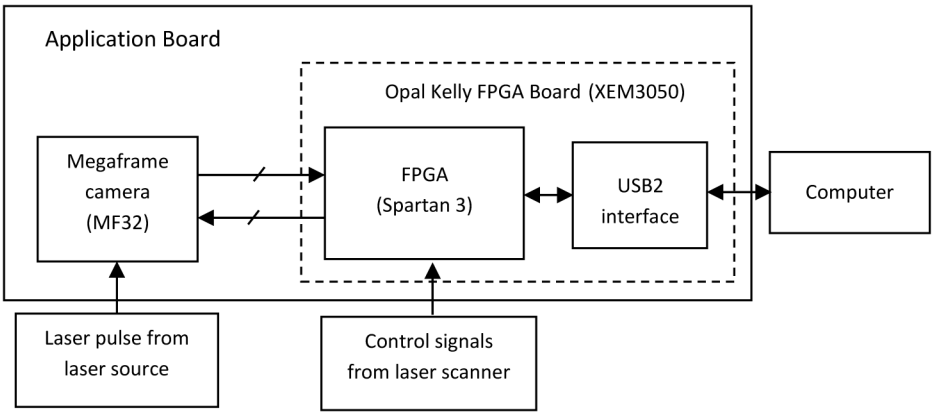

Fig. 3. A typical Megaframe camera based TCSPC system block diagram.

A block diagram of the Megaframe camera is shown in Fig. 4. The Megaframe camera consists of a 32x32 array of pixels which is subdivided into two 32x16 pixel array segments, each served by dedicated readout circuitry. For readout an address decoder selects one row of pixels from each segment simultaneously. Pixels on the selected rows present their 10-bit output data on column buses to broadcast it to serialiser cells located at the top and bottom of the array. One serialiser cell and one I/O pad is assigned to each 16-pixel column in each segment to transmit the data off-chip. Thus, a total of 64 I/O pads, each operating at 80MHz, are used to readout the Megaframe camera at a data rate of 5.12 Gbit/s.

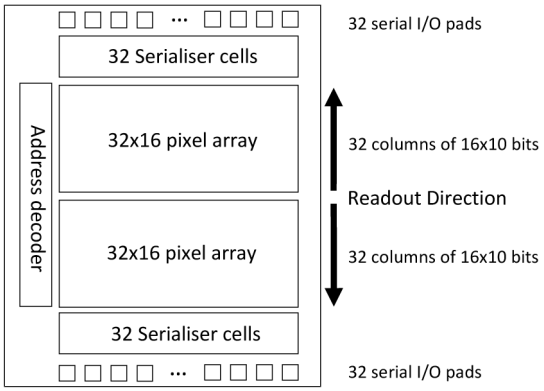

Fig. 4. Megaframe camera block diagram.

3.4 Firmware architecture

A simplified block diagram of the firmware architecture is shown in Fig. 5. The firmware employs 2 deserialiser blocks, one for each segment of 32x16 pixel arrays, for reconstructing the 10-bit data of each pixel. Each desesrialser block receives a 32-bit input data, coming from 32 I/O pads of the Megaframe camera, and generates 32x10-bit deserialised data corresponding to 32 pixels on currently selected pixel row. The deserialised data is then passed to a data select block to determine if the received data corresponds to the selected pixels for CMM computation. Since in this CMM implementation, only a sub-block of 8x8 pixels are being utilised, the deserialised data will need to be discarded when it falls outside the selected pixels (region of interest). This is realised by assigning an address to each pixel of the 8x8 array by using its row and column position within the 32x32 full pixel array. At the same time, a dedicated CMM block is assigned to each pixel of the 8x8 array. The data select block keeps track of the readout rows from the MF32 camera and continuously monitors the

#256784 Received 5 Jan 2016; revised 15 Feb 2016; accepted 5 Mar 2016; published 21 Mar 2016

addresses of the readout pixels. When the received data belongs to one of the pixels of the 8x8 array, it is sent to the corresponding CMM block for CMM computation.

For fast acquisition of CMM, the firmware employs a dedicated CMM block for each pixel of the 8x8 pixel array. The role of the CMM block is to provide accumulated Di, Nc, and Nb terms in Eq. (2) at the end of a frame cycle. These terms are then transferred to a PC via a USB2.0 link and the lifetime data for each pixel is calculated in LabVIEW.

Each pixel of the 8x8 array is used for scanning 32x32 data points for producing 256x256 pixel images. Therefore, a scanner block is used to keep track of the image positions generated by each pixel by assigning 5-bit x and 5-bit y addresses for each scan point. This is then used to record the current image position in the header field associated with each frame of data set. At the end of a frame cycle, a FIFO (first-in first-out) data generation block receives a 48-bit header field (generated by the header generation block), 6-bit pixel no and 42-bit CMM data (ie. 23-bit Di, 13-bit Nc, and 6-bit Nb) from each CMM block. Then the FIFO data generation block sends this data, starting with the header field first, to a 128KB FIFO memory block for temporary storage before being transferred to a PC via a USB2 link for further processing and longer term storage. The data is sent to the FIFO in 16-bit chunks, and hence it takes a total of 195 clock cycles to transfer the data to the FIFO from all 64 CMM blocks, including the 48-bit header field. Once the FIFO is full with data for 252 frames (ie, 96KB), only then its contents are sent to the PC via a USB2 link under the control of the Cypress USB microcontroller on the Opal Kelly board [35]. This ensures more efficient and faster transfer of data from FPGA to PC.

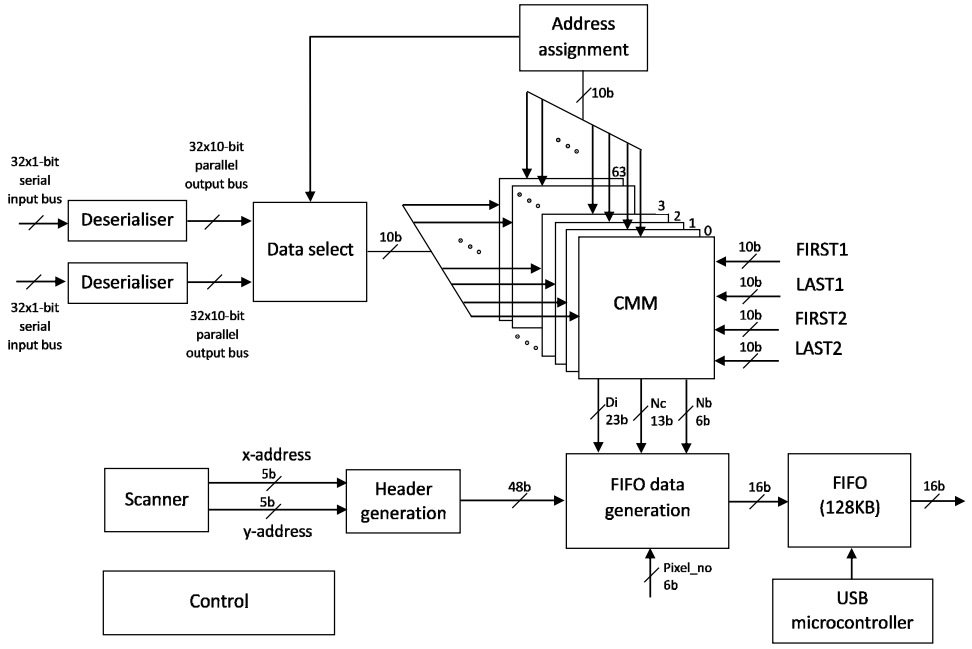

Fig. 5. Firmware block diagram.

3.5 Image acquisition and reconstruction

All aspects of the microscope system including x-y scanner control and synchronization with the Megaframe camera were controlled via custom developed software written in the LabVIEW graphical programming environment. The appropriate region of interest for each sample was first selected whilst operating the microscope in wide-field fluorescent mode. For each individual image acquisition, the system processed 32 × 32 data points for 8 × 8

#256784 Received 5 Jan 2016; revised 15 Feb 2016; accepted 5 Mar 2016; published 21 Mar 2016

detectors producing 256 × 256 pixel images. Lifetime data can be acquired using either TCSPC or CMM modes of operation.

In TCSPC mode, on-pixel TDCs generate raw time-correlated data, which are stored and then post-processed offline to generate an image. More information on TCSPC data acquisition can be found in Poland et al. [15]. Once processed this data is saved and then subsequently analyzed using TRI2 lifetime analysis software [36]. In CMM mode, the lifetime data is determined in real time.

Before operating CMM mode several aspects of the algorithm must be defined by the user. These are the start point and end point bin positions which define the boundaries for the two timing windows, as shown in Fig. 6: (i) Measurement window (mw) for measuring the lifetime of the fluorescence histogram and (ii) Background window (bw) for monitoring the background noise.

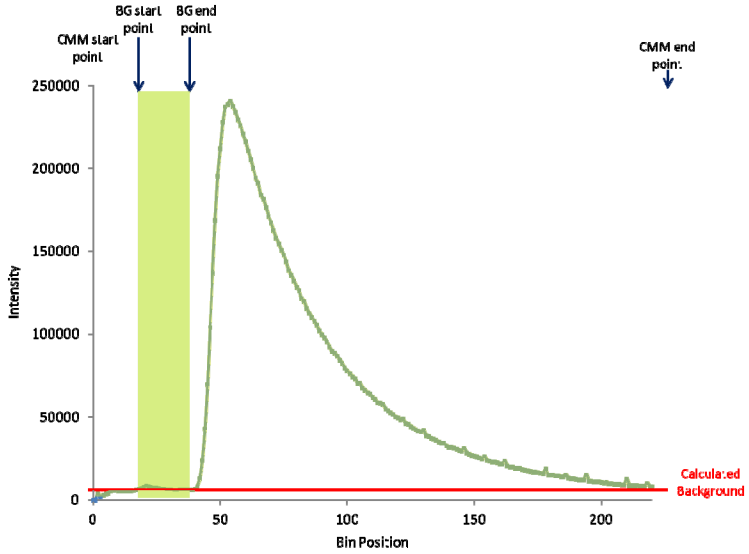

Fig. 6. A typical graph of a measured fluorescence histogram indicating the typical positions of the timing windows for measurement (yellow) and background (green) when set up to acquire data for $CMM_{diffsub}$.

These windows are pre-defined by users by specifying start point and end point time bin position parameters for each window. For the measurement window in $CMM_{original}$, the parameter CMM start point is normally set to the bin providing the highest photon counts and the parameter CMM end point is set such that the width of the window (T = Mh) satisfies the following condition: $T>4\tau$ as described in Li et al. [29]. In $CMM_{diffsub}$, the measurement window is set to the maximum window size as shown in Fig. 6. The background window is positioned before the peak of the measured fluorescence histogram and does not need to be as wide as the measurement window since its purpose is to estimate the average background noise level. The position and width of each window can be easily redefined by users to optimise measurement results.

3.6 Plasmids, cell lines, and cell culture conditions

The mRFP1-eGFP FRET standards are described elsewhere [37]. MCF7 breast carcinoma cells were grown in DMEM medium supplemented with 10% fetal bovine serum (FBS), penicillin G (100 U/ml)/streptomycin (100 mg/ml) and 1% L-glutamine, and cultured in an atmosphere containing 5% CO2/95% air (v/v). Cells were plated with 70% confluence into multiwell chambers (Imaging Chambers CG, PAA Laboratories). 24 hours later, cells were

#256784 Received 5 Jan 2016; revised 15 Feb 2016; accepted 5 Mar 2016; published 21 Mar 2016

transiently transfected with plasmids using a DNA/Fugene6 mixture (Promega, Madison, WI, USA) and were maintained at 37°C in a humidified 5% CO2 atmosphere for additional 24h to allow expression of exogenous proteins. For live cell imaging, cell culture media was replaced with phenol red-free OptiMEM (Gibco), supplemented with 25 mM HEPES. The microscope body was equipped with an environment chamber (Solent Scientific Ltd, UK) enabling cell cultures to be stably maintained at 37°C for the duration of imaging experiments.

4. Results

In order to first evaluate the capability of $CMM_{diffsub}$ algorithm to compensate for increasing background noise it was tested and compared with $CMM_{original}$ for a number of simulated data sets. Setting the lifetime of the transient to 2 ns and incorporating a simulated instrument response function into the model similar to one in our system, transient decays were generated where the % of the background noise to the total number of photons could be modified. For each % background contribution setting, 4096 individual transients were taken and the lifetimes determined using $CMM_{original}$ and $CMM_{diffsub}$. Data analysis showing the % background noise to total number of photons against the calculated average lifetime for each CMM algorithm is presented in Fig. 7.

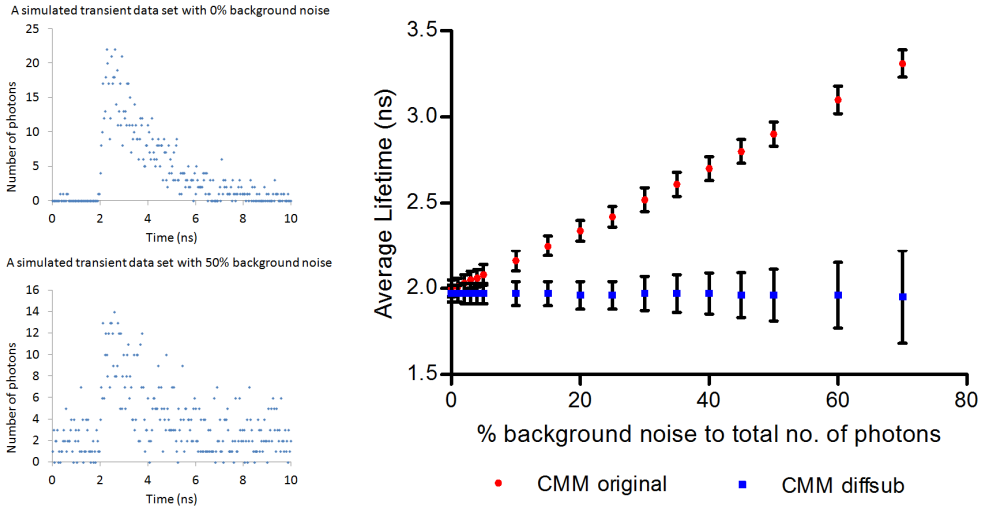

Fig. 7. Analysis of simulated transient data sets showing how increasing the percentage contribution background noise to total number of photons affected the average lifetime value of 4096 transients determined using $CMM_{original}$ and $CMM_{diffsub.}$ For each individual transient, the total number of photons remains constant at 1000 counts.

As the % contribution of background increases, CMM tends to over estimate the lifetime increasing from 2.00 +/– 0.05 ns for 0% background noise up to 3.31 +/ 0.08 ns for 70% background. With $CMM_{diffsub}$, the average lifetime determination is independent to background variation, with an average lifetime changing from 1.97 +/– 0.05 ns to 1.95 +/– 0.27 ns. As one would expect, the errors associated with average lifetime get larger with increasing background levels as the algorithm is using less photons to determine the centre-of-mass.

In order to evaluate the performance of the new $CMM_{diffsub}$ algorithm in a real setting, live cells experiments were performed and lifetimes compared. We imaged live MCF-7 human breast carcinoma cells [38] transiently transfected with FRET standards comprising of eGFP and mRFP1 separated with different amino acid (aa) linker lengths (7aa, 19aa, 32aa) [37]. These different FRET rulers provided the suitable lifetime contrast range required to

#256784 Received 5 Jan 2016; revised 15 Feb 2016; accepted 5 Mar 2016; published 21 Mar 2016

effectively assess the capability of the new CMM algorithm. All 256x256 images were acquired in 10 second acquisitions and lifetime data analysed with 3x3 circular binning.

To assess the effects of the variability of DCR between Megaframe pixels on lifetime determination using CMM techniques, lifetime data sets for $CMM_{original}$, CMM_{diff} and $CMM_{diffsub}$ were calculated. The associated intensity, lifetime and composite images for cells expressing the various FRET standards are compared in Fig. 8.

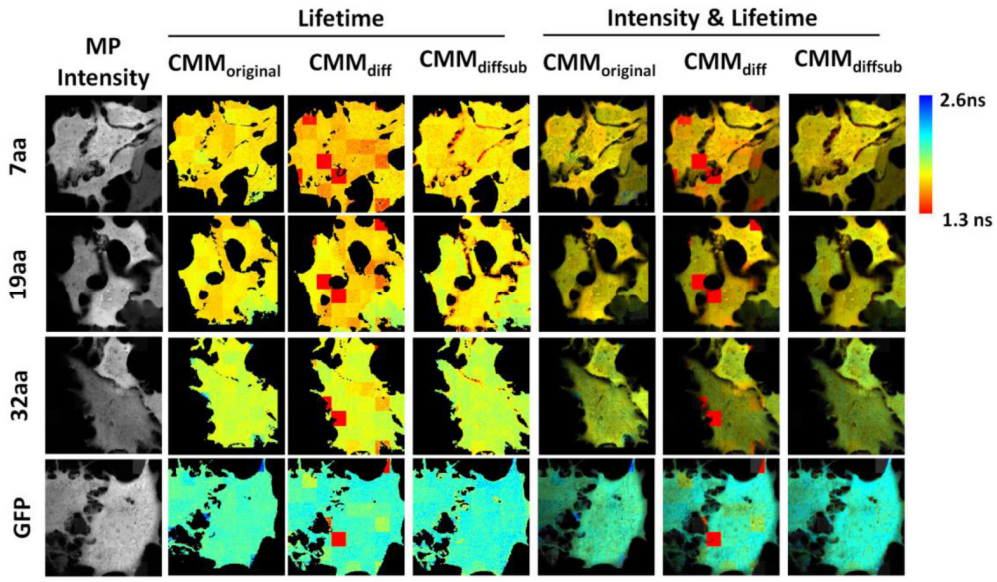

Fig. 8. Comparison of various CMM approaches to lifetime determination for live MCF-7 breast cancer cells expressing FRET standards imaged at 10 second time frames. Each standard (7aa, 19aa, 32aa) is comprised of eGFP and mRFP separated with different length amino acid linker sequences which are denoted by the number. These are then compared with cells expressing eGFP alone. Intensity, lifetime and composite images of live cells expressing the FRET standards and eGFP are presented.

As expected the FRET efficiencies E (defined as $E = 1- (\tau_{Donor\ \&\ Acceptor} / \tau_{Donor})$) were shown to increase as the linker size decreases with data. The FRET standards used for this experiment are non-functional and therefore one would expect the lifetime to be uniform throughout all of each cell. Thus in both $CMM_{original}$ and CMM_{diff} the lifetime variation is dependent on the detector, with an increase in disparity coinciding with an increase in DCR.

In Fig. 9, the lifetime distributions for a number of detectors were plotted on histograms and compared for each CMM technique. Whilst the disparity in lifetimes between detectors for $CMM_{original}$ can be clearly seen both visually and in the associated histogram, this disparity is much worse for CMM_{diff}. Incorporating background subtraction reduces this disparity dramatically and the lifetime distributions of each pixel align. The issues associated with CMM_{diff} pixel variability is due to the greater sensitivity of the τ_{CMM} of the IRF to the background signal level. By incorporating a mechanism to remove background, a more accurate determination of lifetime is achieved which is insensitive to individual detector characteristics as seen in $CMM_{diffsub}$.

#256784 Received 5 Jan 2016; revised 15 Feb 2016; accepted 5 Mar 2016; published 21 Mar 2016

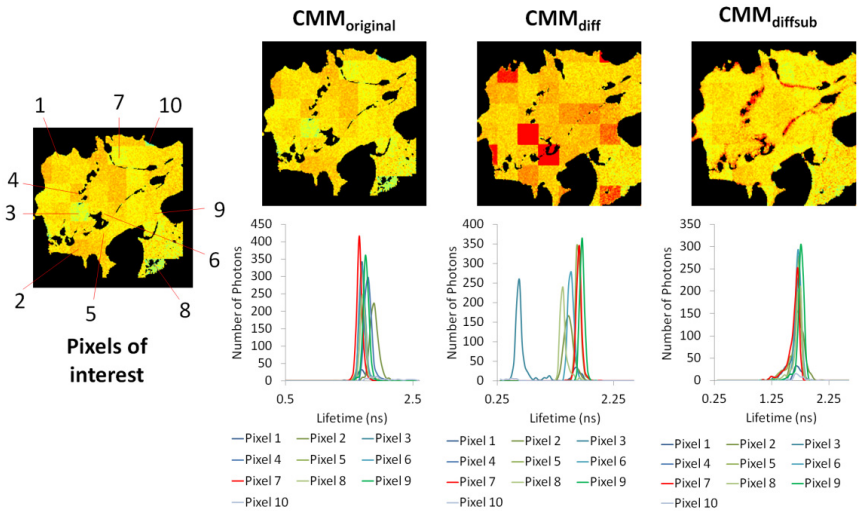

Fig. 9. Comparison of various CMM approaches to lifetime determination. These were Original CMM, Differential CMM, and Differential CMM incorporating background subtraction approaches for lifetime determination for a live MCF breast cancer cell expressing the eGFP-7AA-mRFP FRET standard. Of the 8x8 detector array used to acquire the image, individual histograms associated with 10 SPAD detectors were chosen as displayed in the pixels of interest image and presented for each CMM variant.

The $CMM_{diffsub}$ lifetime determination algorithm was further compared to the least-squares fitting Levenburg-Marquardt (L-M) approach and time-gated rapid lifetime determination (RLD) approach to measure its performance. Analysing TCSPC data with L-M is usually considered the gold standard for lifetime determination whilst RLD is the most commonly used analysis technique for real-time FLIM in gated image intensifier (GOI) based FLIM systems. Comparing $CMM_{diffsub}$ with these two alternative approaches will give a clear indication as to how accurate the algorithm is and how well it performs. RLD analysis was performed on raw TCSPC data with the size and position of the two gates optimised to provide the best performance for the range of lifetimes measured. Data sets were taken of live cells expressing the FRET standards and the results presented in Fig. 10.

#256784 Received 5 Jan 2016; revised 15 Feb 2016; accepted 5 Mar 2016; published 21 Mar 2016

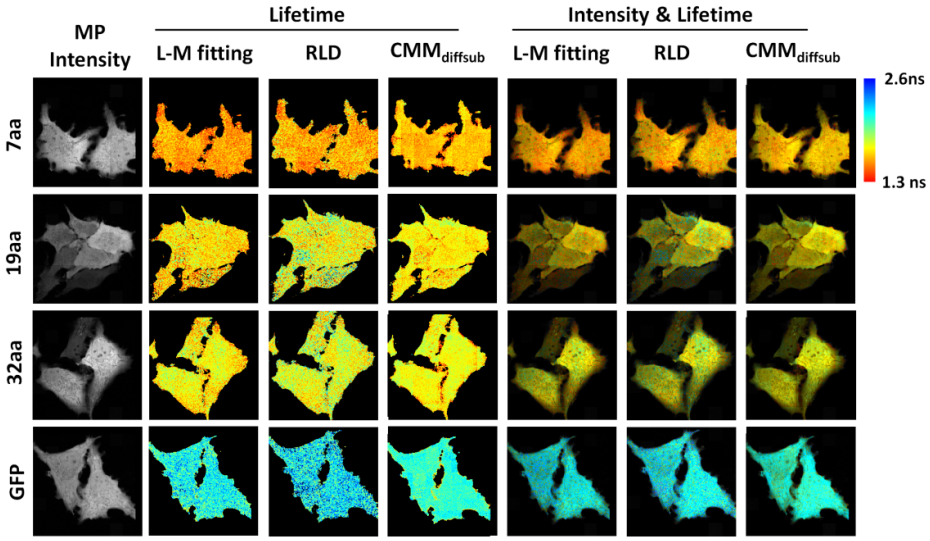

Fig. 10. Comparing Levenburg-Marquardt (L-M), Time gated Rapid lifetime determination (RLD) and Centre-of-Mass Method (CMM) lifetime determination techniques with data sets taken from live MCF-7 breast cancer cells expressing FRET standards imaged at 10 second time frames.

Unlike CMM$_{diffsub}$ and L-M fitting (for which background subtraction is also performed), RLD calculation does not take into account the background signal and therefore the resulting disparity in lifetime between individual detectors (Fig. 10) can be clearly seen. Data taken with the CMM$_{diffsub}$ approach was shown to correlate very strongly with L-M fitting data (Fig. 11) giving a Pearson's coefficient of 0.92 and provided a more accurate determination than time-gated RLD.

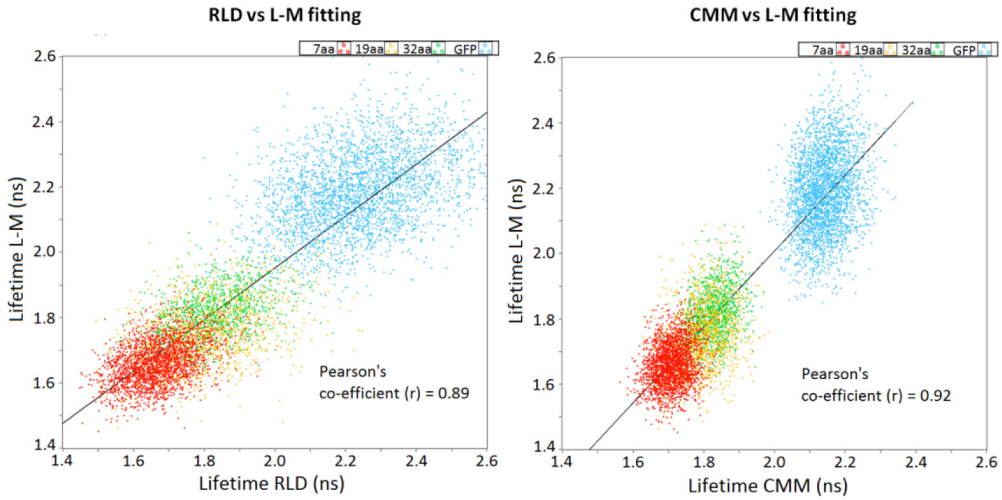

Fig. 11. Examining the correlation of RLD and CMM to the L-M fitting approach for lifetime determination on a pixel comparison basis for data presented in Fig. 10. For each data set the 7aa data is presented as red, 19aa data is yellow, 32aa data is green and the eGFP only data is blue. The Pearson product-moment correlation coefficient is used to determine the correlative significance.

#256784 Received 5 Jan 2016; revised 15 Feb 2016; accepted 5 Mar 2016; published 21 Mar 2016

CMM data sets actually have a tighter distribution of lifetimes (Fig. 12) than the L-M analysed counterparts which may be explained by the background subtraction methods used. For CMM, a more accurate value of the background was determined as all the data for each pixel was used to calculate it, whereas for L-M, only the pre-pulse data for the transient which was being analysed at the time was used.

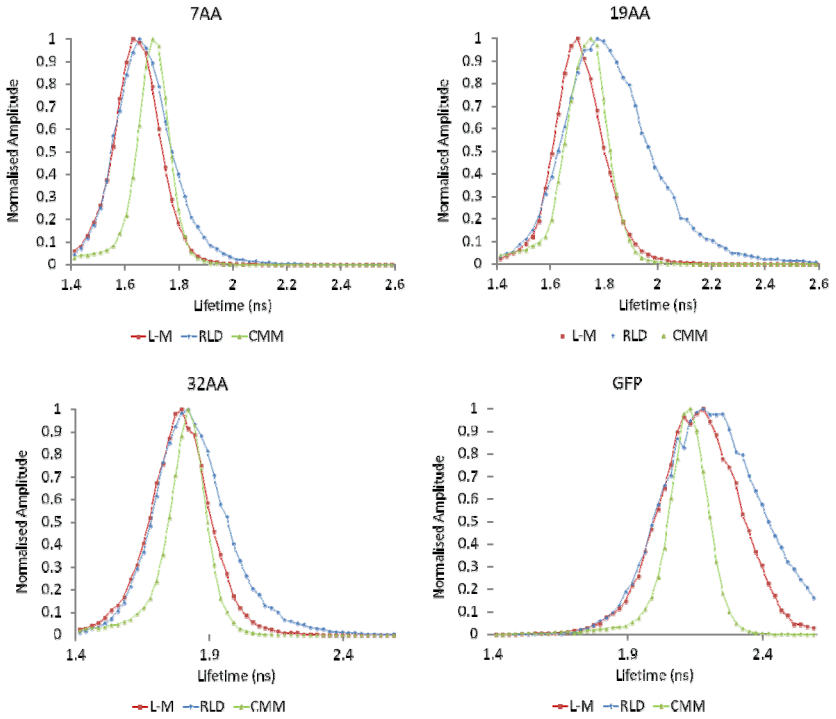

Fig. 12. Histograms showing the distribution of lifetimes determined using RLD, CMM and L-M for 7aa, 19aa, 32aa and GFP data sets presented in Fig. 10 are shown.

Taking eGFP as the donor only lifetime, for each cell the FRET efficiencies were calculated and statistical analysis was performed (see Fig. 13 and Table 1).

#256784 Received 5 Jan 2016; revised 15 Feb 2016; accepted 5 Mar 2016; published 21 Mar 2016

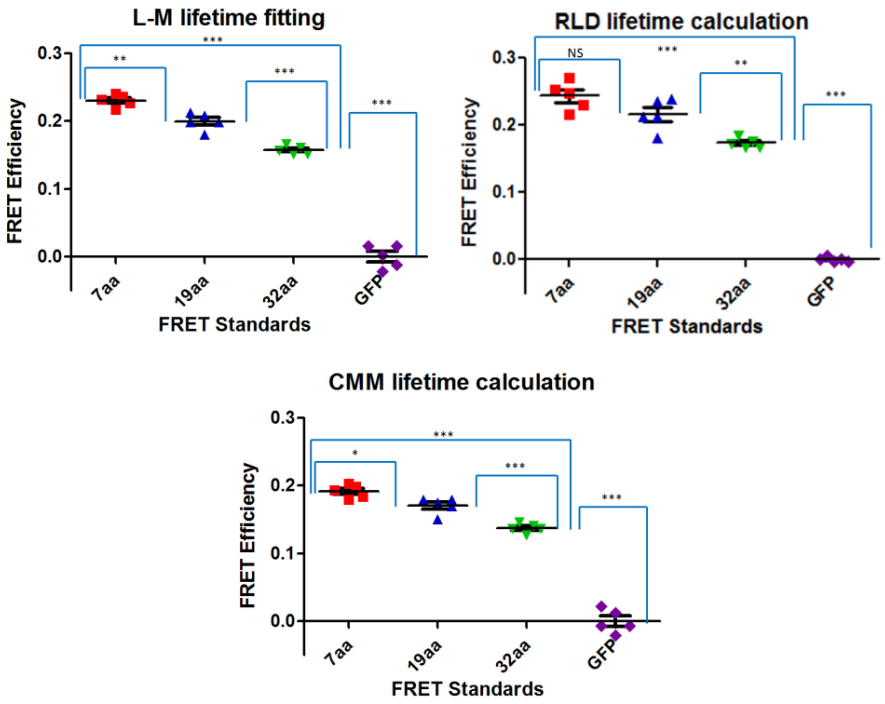

Fig. 13. Statistical analysis comparing the average FRET efficiencies for a sample of 5 cells expressing each FRET standard and eGFP are presented for each lifetime determination technique. In order to compare two different populations for significance the unpaired Student t-test was used. *** between populations denotes a highly significant difference in lifetime values ($p<0.001$), ** denotes a very significant difference in lifetime values ($p\leq0.01$), * denotes a significant difference in lifetime values ($p<0.05$) and NS denotes no significance ($p>0.05$).

Table 1. The calculated FRET efficiencies for each technique are displayed

Transfection	GFP CaaX	GFP_32aa_RFP	GFP19aa_RFP	GFP_7aa_RFP
FRET efficiency L-M Fitting	0	0.157 ± 0.006 N = 5	0.200 ± 0.013 N = 5	0.231 ± 0.009 N = 5
FRET efficiency RLD	0	0.173 ± 0.007 N = 5	0.220 ± 0.023 N = 5	0.243 ± 0.021 N = 5
FRET efficiency $CMM_{diffsub}$	0	0.137 ± 0.007 N = 5	0.171 ± 0.012 N = 5	0.192 ± 0.010 N = 5

As one would expect from Fig. 13, L-M fitting provided the most accurate means to distinguish between FRET standard populations (corresponding to $P \leq 0.001$) between 19aa, 32aa, and eGFP and a high significance ($P \leq 0.01$) between 7aa and 19aa populations. The $CMM_{diffsub}$ algorithm provided the next accurate approach whilst RLD was the least accurate method, where in one case significance between 7aa and 19aa populations could not even be determined ($P > 0.05$). These results demonstrate that $CMM_{diffsub}$ gives a much more accurate determination of the lifetime per pixel than RLD. It should be noted that this comparison using RLD is at Poisson limited signal to noise which is superior to what one would expect from GOI performance.

The discrepancy in FRET efficiencies between L-M and CMM could be accounted for by the assumption that these FRET standards follow a single exponential decay model – EGFP has been shown to have more complex decay kinetics and the FRET behaviour may be far from simple [39]. We are also assuming that the linkers are stiff, holding the fluorescent proteins at a fixed distance from each other with no preferred orientation (we would expect

#256784 Received 5 Jan 2016; revised 15 Feb 2016; accepted 5 Mar 2016; published 21 Mar 2016

this assumption of rigidity to fail for long linkers (32aa) and for orientational effects to be more pronounced for short linkers (7aa)).

5. Discussion and conclusions

This paper presents the development of a new type of centre-of-mass approach incorporating background subtraction for real-time lifetime determination. We have demonstrated that in comparison to other CMM algorithms and time-gated RLD it offers significant advantages in terms of lifetime accuracy and insensitivity to variability in DCR between Megaframe camera pixels. Unlike other RLD algorithms (i.e. Time gated), no prior knowledge of the expected lifetime is required to perform lifetime determination. Whilst not as accurate as TCSPC mean squared fitting techniques such as Levenburg-Marquardt, the ability of this technique to provide real-time lifetime readout makes it extremely useful for a number of applications. Calculation of the lifetime on-FPGA reduces the data transfer requirements of the system allowing the Megaframe camera to operate at the maximum photon collection rate of 500kilocounts / pixel / second which is determined by the FPGA firmware.

Acknowledgments

The authors would like to thank: The Biotechnology and Biological Sciences Research Council UK (BB/I022074/1 and BB/I022937/1); STMicroelectronics (Imaging Division, Edinburgh, UK); Cancer Research UK, Engineering and Physical Sciences Research Council (UK) (Interdisciplinary Research Collaboration grant EP/K03197X/1), Medical Research Council (UK) (MR/K015664/1) and Department of Health (UK), KCL/UCL Comprehensive Cancer Imaging Centre; Dimbleby Cancer Care endowment fund to King's College London and The Royal Society. The Megaframe project has been supported by the European Community within the Sixth Framework Programme IST FET Open, http://www.megaframe.eu.

#256784 Received 5 Jan 2016; revised 15 Feb 2016; accepted 5 Mar 2016; published 21 Mar 2016